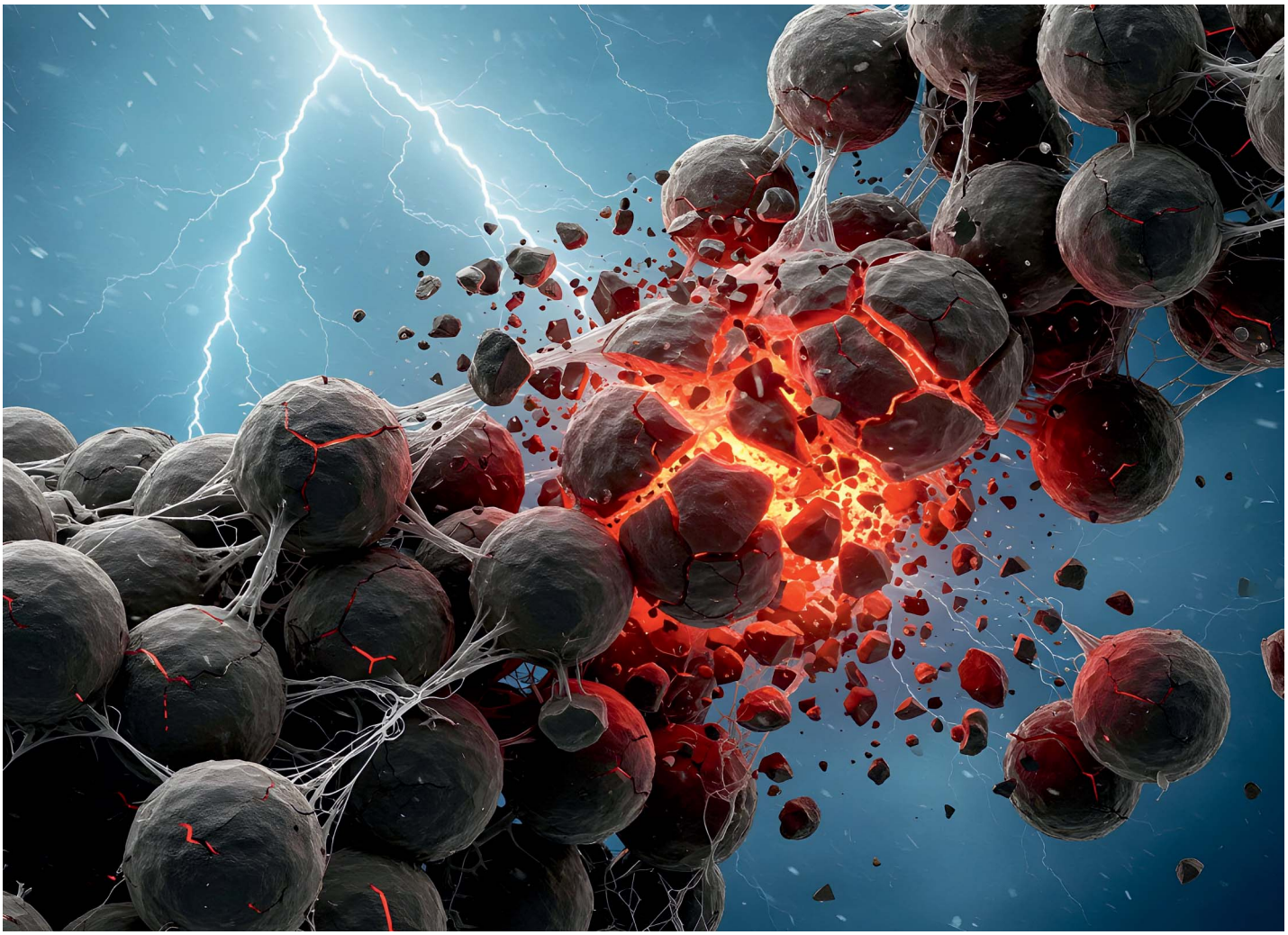

Highlighting research on particle fracture in solvent-free electrodes for Li-ion batteries led by Dr Guillaume Matthews at the Department of Materials, University of Oxford, UK.

Impact of binder content on particle fracture and microstructure of solvent-free electrodes for Li-ion batteries

Solvent-free electrodes, also known as dry-processed electrodes, have a unique microstructure composed of active material particles held together by a web-like network of PTFE nano-fibrils. The fraction of binder in these electrodes has a dramatic impact on their processability and mechanical properties, ultimately controlling their microstructure and electrochemical performance. The origin of particle fracture was linked to the viscoelastic response of the electrode during compression, with lower binder content leading to higher electrode ductility and a reduction of active material fracture during the manufacturing process.

Image reproduced by permission of Guillaume Matthews from *J. Mater. Chem. A*, 2025, **13**, 18283.

As featured in:

See Guillaume Matthews *et al.*, *J. Mater. Chem. A*, 2025, **13**, 18283.

ROYAL SOCIETY OF CHEMISTRY

rsc.li/materials-a

Registered charity number: 207890

Journal of Materials Chemistry A

ROYAL SOCIETY OF CHEMISTRY

COMMUNICATION

View Article Online
View Journal | View Issue

Cite this: J. Mater. Chem. A, 2025, 13, 18283

Received 10th March 2025
Accepted 6th May 2025

DOI: 10.1039/d5ta01950h

rsc.li/materials-a

Impact of binder content on particle fracture and microstructure of solvent-free electrodes for Li-ion batteries†

Guillaume Matthews, *[ad] Benjamin Meyer, [ad] Christopher Doerrer,[b] Julia Ramírez-González,[a] Ed Darnbrough, [ad] Noël Hallemans,[cd] David Armstrong[ad] and Patrick S. Grant[ad]

The fraction of polytetrafluoroethylene (PTFE) binder in solvent-free electrodes for Li-ion batteries, also known as dry-processed electrodes, is shown to have a dramatic impact on their processability, microstructural evolution and electrochemical performance. We show experimentally that increasing the binder fraction from 0.5 to 4 wt% transformed the electrode microstructure from an effective, open structure containing PTFE nano-fibrils to a compact morphology with fragmented active material and porosity blocked by PTFE agglomerates. The solvent-free electrodes showed a classic visco-elastic response during compression, comprising three distinct regions of deformation. The electrode stiffness and yield strength increased non-linearly with binder fraction such that for higher binder contents (>2 wt%), there was extensive $LiNi_{0.6}Co_{0.2}Mn_{0.2}O_2$ (NMC) particle fracture during the calendering process, with cracks propagating along the grains of polycrystalline NMC particles. Conversely at lower binder fraction (<2 wt%), PTFE readily fibrillated into highly textured (100) crystalline nano-fibrils and NMC particles remained largely intact. These electrodes showed superior electrochemical performance due to higher ionic mobility through the open nano-fibrillar microstructure and intact NMC particles.

1 Introduction

Electrodes for commercial Li-ion batteries (LIBs) are manufactured by slurry casting, a process that has become synonymous with LIB manufacturing since their commercial rise in the 1980's. Slurry casting lines have become progressively larger and faster (up to 1 m width and 90 m min^{-1}), but the key steps of the LIB electrode manufacturing process itself have remained essentially the same.[1] Although casting is highly productive, it also has several inherent limitations such as high energy consumption (and associated high embedded carbon), extensive use of flammable and highly toxic solvents (especially for the positive electrode), and large capital and operational costs that are mostly due to solvent drying and recovery steps.[2,3] Recently, solvent-free processing methods for LIB electrodes have gained attention from both industry and research laboratories, with potential advantages over slurry casting in terms of sustainability, cost and safety due to the complete elimination of solvents.[4–8] Moreover, solvent-free electrodes can show better electrochemical performance than conventional slurry cast electrodes.[9–11]

Amongst the different solvent-free processes, those that are based on polytetrafluoroethylene (PTFE) fibrillation, to replace the popular *N*-methyl-2-pyrrolidone (NMP)/polyvinylidene fluoride (PVDF) binder system, have attracted the most interest, with pilot and industrial lines already in operation.[12,13] However, despite the growing interest in solvent-free processing, significant manufacturing challenges have emerged, hindering the continued roll-out of solvent-free electrodes for commercial LIBs. A recent teardown of Tesla's latest 4680 cell revealed that the graphite anode appeared to be manufactured by a solvent-free process using PTFE binder.[14] In contrast, the cathode was made by slurry casting using a traditional PVDF binder.

The PTFE fibrillation approach can produce functioning LIB electrodes with a range of active materials including $LiNi_{0.6}Co_{0.2}Mn_{0.2}O_2$ (NMC), $LiFePO_4$ (LFP) and $LiMn_2O_4$ (LMO).[9,15–22] However, there is a lack of understanding of how the PTFE fraction impacts overall processability and active material integrity, and subsequent electrochemical response. Although there are performance benefits in using as low as 0.2 wt% PTFE for all-solid-state-battery composite cathodes,[23,24] most LIB electrodes contain a much higher fraction of binder (2–10 wt%) and have comparatively large thicknesses ranging from 150 up

[a]Department of Materials, University of Oxford, Parks Road, OX1 3PH, Oxford, UK. E-mail: guillaume.matthews@materials.ox.ac.uk

[b]Department of Mechanical and Industrial Engineering, University of Toronto, Canada

[c]Department of Engineering Science, University of Oxford, Parks Road, OX1 3PJ, Oxford, UK

[d]The Faraday Institution, Quad One, Harwell Science and Innovation Campus, Didcot, UK

† Electronic supplementary information (ESI) available. See DOI: https://doi.org/10.1039/d5ta01950h

to 400 μm, as summarised in Fig. S.1.† Such thick electrodes generally offer poor power densities, even at charge–discharge rates as low as C/5, making them impractical for electric vehicles (EV) and portable electronics.[25]

In this paper, we investigate systematically the impact of binder content on the processability and microstructure of PTFE-based solvent-free electrodes with a practical thickness of 100 μm, and thinner than commonly reported. We present detailed characterisation at a range of scales to reveal how higher binder contents fail to fibrillate properly and lead to local stresses that cause extensive active material fracture and subsequent poor electrochemical performance. We introduce a mechanistic explanation of how particle fracture relates to the viscoelastic properties of the solvent-free electrodes and its impact on the electrode microstructure. We also report the first analysis of individual PTFE nano-fibrils *via* ultra-low dose transmission electron microscopy (TEM), providing further insight into the conditions for the critical formation of PTFE nano-fibrils.

2 Results and discussion

2.1 Microstructure evolution

Electrodes with different PTFE binder fractions (from 0.5 to 4 wt%) were produced by a conventional solvent-free method (described in the ESI†), and then calendered to a thickness of approximately 100 μm, as depicted in Fig. 1A. All the electrodes contained 3.5 wt% carbon nano fibres (CNF) to provide electrical percolation, with NMC active material making up the balance. Fig. 1B and C show secondary electron (SE) scanning electron microscopy (SEM) images of the top view of the typical electrode microstructure containing 0.5 and 4 wt% PTFE binder, respectively. The 0.5 wt% PTFE electrode in Fig. 1B showed relatively large, open porosity with NMC particles

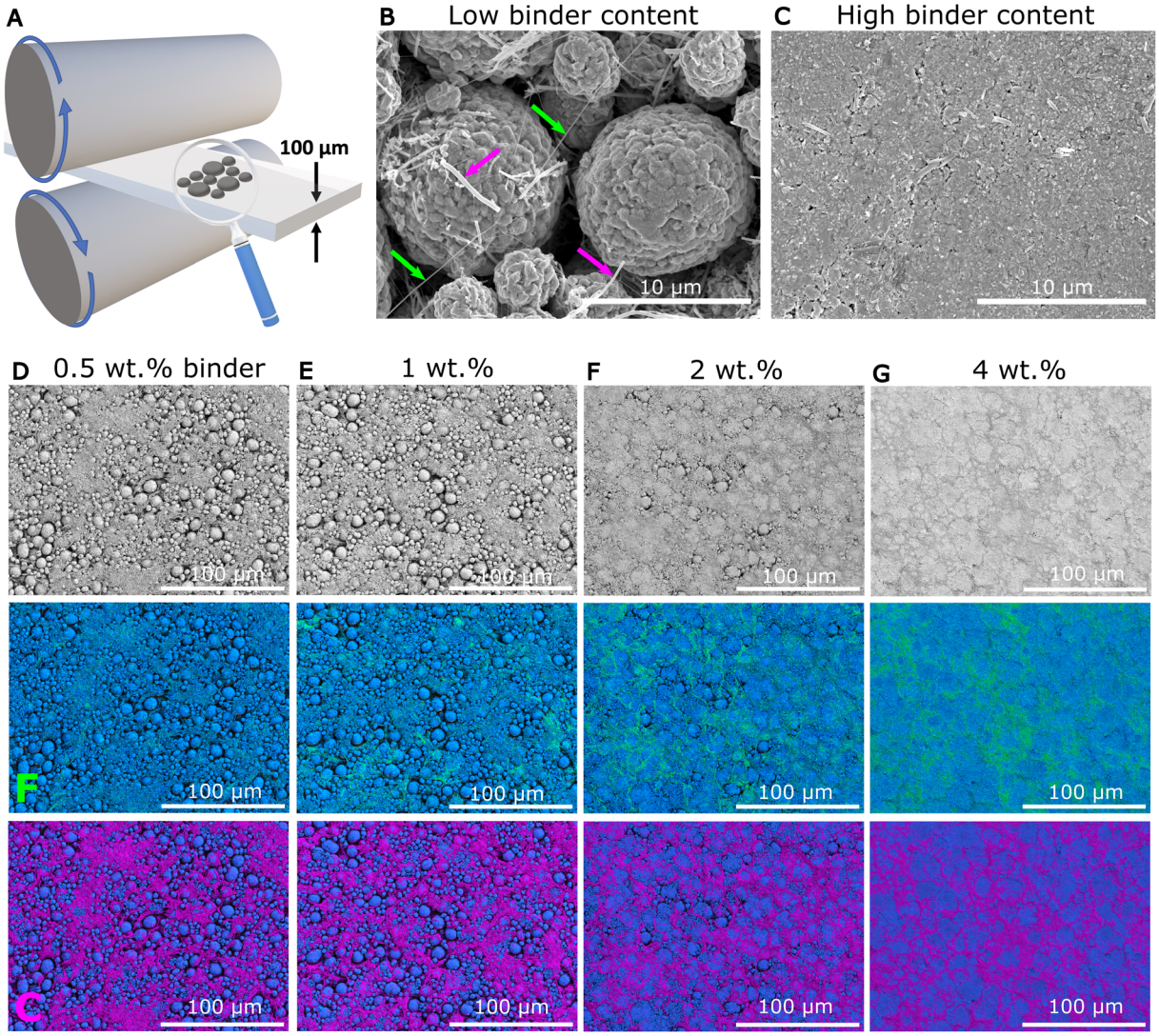

Fig. 1 (A) Schematic of the electrode calendering process. (B and C) SEM micrographs of NMC electrodes containing 0.5 and 4 wt% PTFE, respectively. (D–G) (Top) SEM micrographs of NMC electrodes containing 0.5, 1, 2 and 4 wt% PTFE, respectively. Middle: corresponding EDX maps showing the active material (Ni–O signal) and binder (F signal) in blue and green, respectively. (Bottom) EDX maps showing the active material (Ni–O signal) and carbon additive (C signal) in blue and pink, respectively.

(diameter 4–10 μm) and PTFE fibrils (green arrows) up to 100 μm in length spanning several particles, consistent with previous reports.[10] The CNFs are highlighted by the pink arrows. In contrast, the 4 wt% electrode in Fig. 1C showed very significantly less open surface porosity. The series of lower magnification SE images (top row) in Fig. 1D–G for 0.5, 1, 2 and 4 wt% PTFE electrodes confirmed the progressive reduction of surface porosity. Macroscopic density measurements indicated a reduction in bulk porosity from 34% to 20% as PTFE increased from 0.5 wt% to 4 wt% (Fig. S.2†).

Energy dispersive X-ray (EDX) mapping was performed to identify the different electrode constituents. The F maps in Fig. 1D–G (middle row) reveal the binder distribution, while the C maps (bottom row) show the CNFs distribution. The PTFE fibrils for 0.5 wt% PTFE were extremely fine (several tens of nm) and mostly too small to be detected by EDX. Increasing the binder fraction led to thicker fibrils (100 nm up to 1–2 μm) and some larger PTFE regions (1–5 μm) in the 2 wt% electrodes. There were large patches (up to 10–20 μm) of PTFE at the surface of the 4 wt% PTFE electrode. The distinctive features found in the low and high binder content electrodes, were studied further to unravel the details of the PTFE nano-fibrils and the larger surface PTFE regions.

Previous work reported PTFE fibrils with very high aspect ratios and diameters estimated by SEM as fine as 20–50 nm.[10] A typical example of these nano-fibrils is shown in Fig. 2A. Despite the central role of PTFE nano-fibrils in mechanically stabilising solvent-free electrodes, there is surprisingly little reported about their structure. Fig. S.3† shows the XRD pattern of the feedstock PTFE powder with strong Bragg reflections (suggesting a high degree of crystallinity) indexed to the pseudo-hexagonal phase represented schematically in Fig. S.4.† Fig. 2B shows a bright field image of a single PTFE fibril oriented to give strong diffraction contrast. Fig. 2C shows the selected area electron diffraction (SAED) pattern with sharp (100) and (200) Bragg reflections, corresponding to a crystal plane spacing of 4.95 Å and 2.48 Å, respectively. This suggests a highly oriented crystal structure along (100) planes. In contrast to the feedstock powder, there were no pyramidal and basal planes reflections, indicating a strong texture along the [100] direction with fibrillation occurring mainly *via* chains sliding along (100) slip planes.[26]

The cross-section of a 4 wt% PTFE electrode was investigated after Ar ion-milling and the F EDX map in Fig. 2D shows the binder location in green. Consistent with the top view observation in Fig. 1G, there were patches of bulk PTFE at the surface and also throughout the electrode interior. Fig. 2E shows an SEM image obtained using an energy selective back-scattered detector (EsB) to enhance chemical contrast, and revealed that the microstructure was composed of fractured NMC

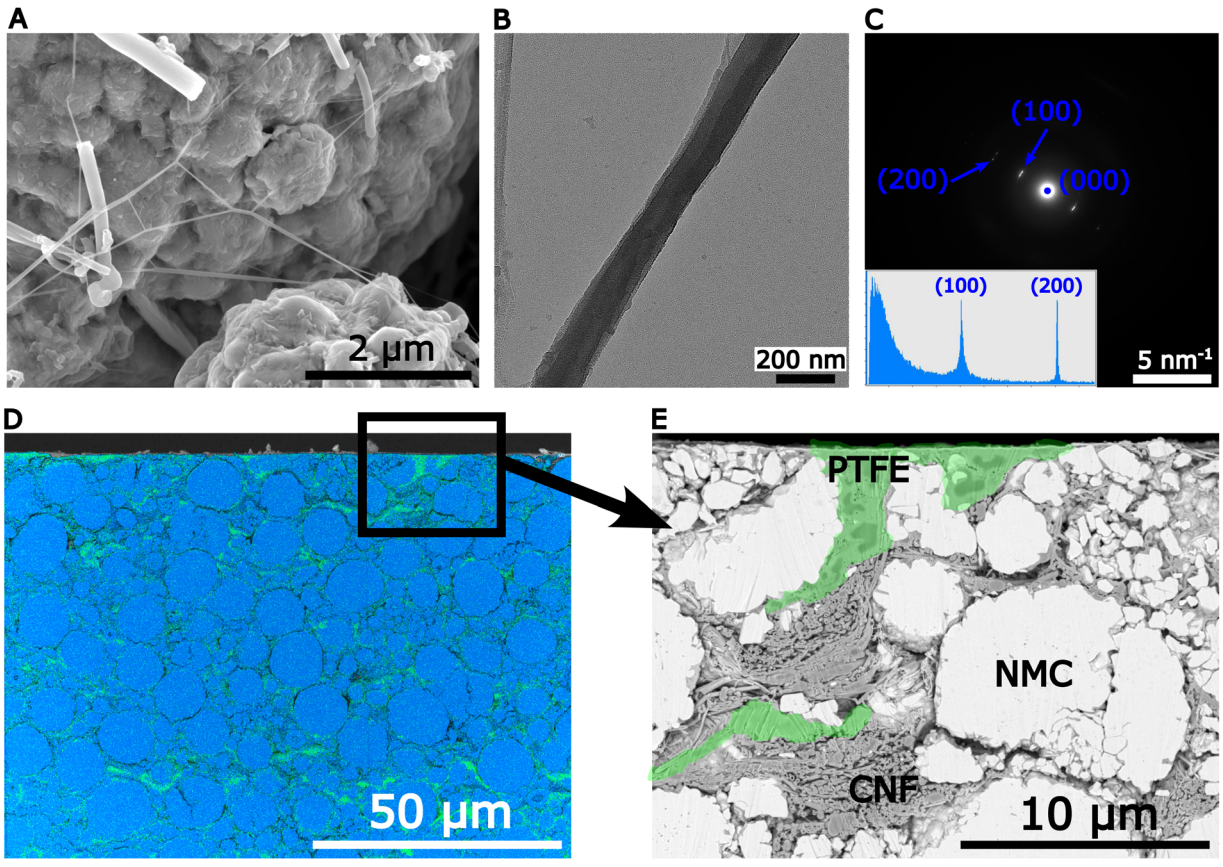

Fig. 2 (A) Secondary electron micrograph of a solvent-free electrode containing 0.5 wt% PTFE. (B) Bright field TEM image of an individual PTFE fibril. (C) Corresponding selected area diffraction pattern and radial intensity profile (inset). (D) F (green) and Ni–O (blue) EDX map of a solvent-free electrode containing 4 wt% PTFE. (E) Energy selective backscattered micrograph of a solvent-free electrode containing 4 wt% PTFE.

particles partially cemented together by PTFE, and CNF agglomerates.

2.2 Active material particle fracture

Given the suggestion that the fraction of binder had a significant impact on NMC particle fracture, NMC morphology was investigated in detail for the 0.5 and 4 wt% PTFE electrodes by digital image analysis of ~5600 particles. Individual NMC particles were identified from EsB images by grey scale segmentation and their segmented morphology was then analysed using algorithms developed in MATLAB. Fig. 3A and B show typical images for low and high binder electrodes respectively, and the corresponding segmented images are shown in Fig. 3C and D, with significantly more particle fracture in the high binder electrode. To quantify this effect, Fig. 3E shows the particle size distributions for both electrodes, with a much greater fraction of particles with diameters <2 μm in the high binder electrode. In contrast, the low binder electrode had two distinct diameter populations, one at ~10 μm and the other one at 3–4 μm. This further suggests that NMC particles underwent significant fracture during calendering of electrodes with high binder fraction. A broken NMC particle is shown in more detail in Fig. 3F with cracks following grain boundaries (highlighted by the orientation sensitive channelling contrast). Fracture of polycrystalline NMC is well-known to degrade subsequent electrochemical cycling behaviour.[27,28] Corresponding XRD patterns of the electrodes containing between 0.5 wt% and 4 wt% PTFE are shown in Fig. 3G, with the well-characterised NMC crystal structure (Fig. 3H) readily indexed for all electrodes. The NMC crystallite size was estimated from the XRD patterns using Rietveld analysis. Fig. 3I shows there was a progressive decrease in crystallite size from 90 nm to 50 nm with increasing binder fraction.

This suggests that in addition to secondary particle fracture, some primary NMC particles might also sustain damage during the calendering process in electrodes containing a high (>2 wt%) fraction of binder.

In summary, detailed SEM investigation showed that increasing the PTFE binder fraction had a significant effect on the tendency of secondary NMC particles to fracture during

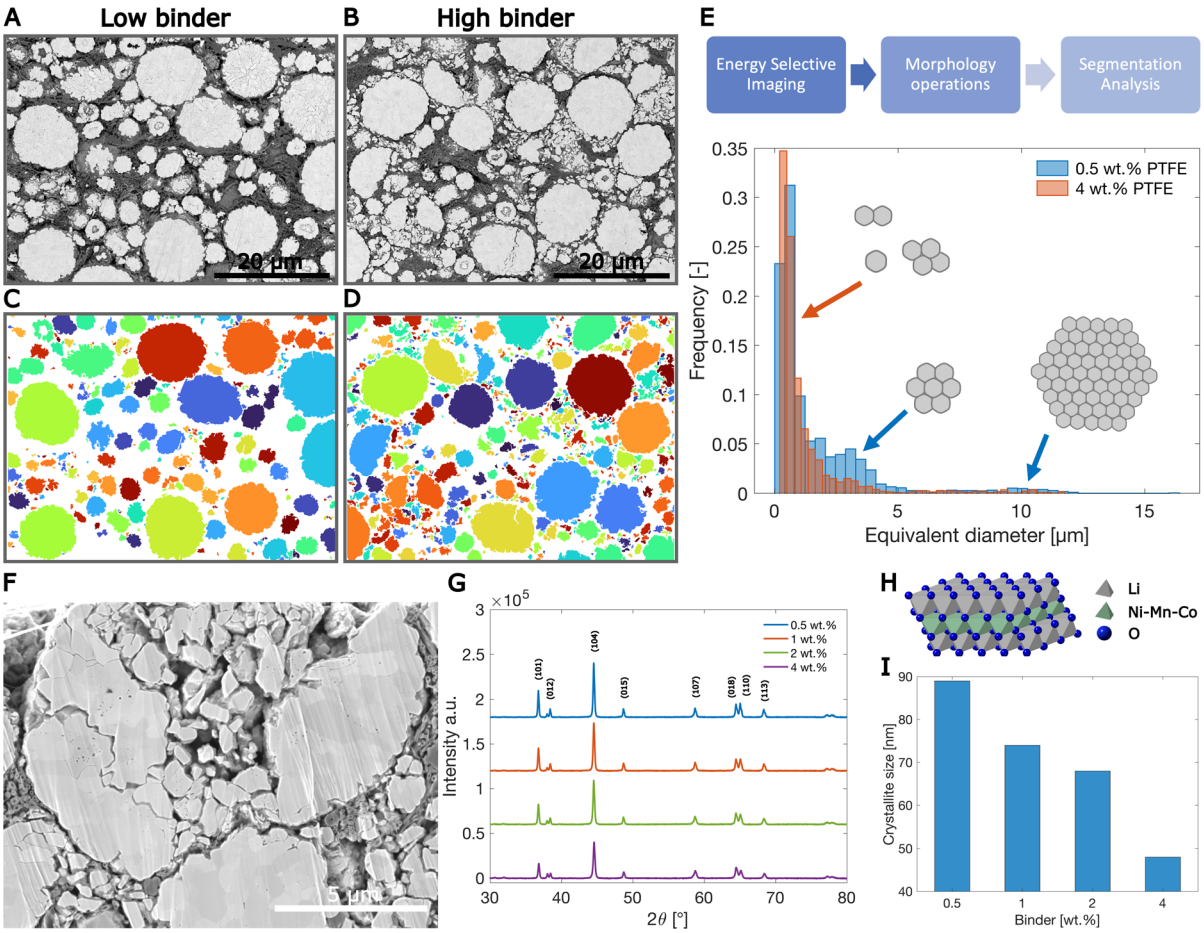

Fig. 3 (A and B) Typical energy selective backscattered micrographs of electrodes containing 0.5 wt% (low) and 4 wt% (high) binder. (C and D) Corresponding segmented images of the NMC particles. (E) Method and histogram showing the NMC particle size distribution for electrodes containing 0.5 wt% and 4 wt% PTFE, 5600 particles were analysed. (F) SE micrograph revealing intergranular fracture of the NMC particles. (G) XRD patterns of electrodes containing 0.5, 1, 2 and 4 wt% PTFE. (H) Crystal structure of the indexed phase for NMC622. (I) Crystallite size evolution with increasing binder fraction.

calendering, even though PTFE based solvent-free electrodes are usually assumed to deform readily at a processing temperature of 80 °C.

2.3 Viscoelasticity at the origin of particle fracture

To understand the relationship between NMC particle fracture, binder fraction and process conditions, uniaxial compression and direct image correlation were used to investigate the mechanical properties of small cylinders (2 mm height × 5 mm diameter) with the same fabrication history and composition as the solvent-free electrodes, as shown schematically in Fig. 4A. The cylinder dimensions were tracked in real time during compression to obtain the true stress–true strain curves shown in Fig. 4B. Binder fraction had a very strong influence on electrode mechanical properties with three deformation regimes identified: (i) an elastic linear region, followed by (ii) a non-linear ductile plateau in which the PTFE flowed, and (iii) a highly non-linear region of rapidly increasing applied stress corresponding to compaction.[29]

It was assumed that in this region particles became interlocked due to local friction and particle fracture occurred, if local stresses were sufficiently high. Fig. 4C shows that the electrode Young's modulus and yield strength increased non-linearly from 10 MPa to 30 MPa and from 1 MPa to 2.5 MPa respectively by increasing the binder from 0.5 wt% to 4 wt%. Fig. 4D shows the normalised volume evolution with deformation for low and high binder electrodes. After a similar elastic loading region (A), there was a rapid volume reduction for the high binder electrode, indicating a compaction regime. In contrast, the low binder electrode maintained a constant volume suggesting an extended region of flow.[30]

Overall, electrodes containing 0.5 wt% PTFE underwent significant plastic deformation without damaging the NMC particles, as schematically shown in Fig. 4E. On the other hand, electrodes with 4 wt% PTFE required much higher stress to achieve similar deformations (240% higher at 80% strain), causing NMC particles to fracture, as shown schematically in Fig. 4F. Apart from NMC, particle fracture during manufacturing is known for $LiNi_{0.8}Co_{0.15}Al_{0.05}O_2$ (NCA) and can be expected for most commercial active materials.[20] Our results suggest that relatively low fractions of binder (<1 wt%) lead to electrodes with greater formability which drastically reduces active material fracture during the calendering process.

2.4 Impact on electrochemical performance

Fig. 5A shows the first formation charge–discharge (C/20) cycle of 0.5, 1, 2 and 4 wt% PTFE electrodes, and a typical capacity for NMC of ~170 mA h g^{-1}. At very low C-rate, the system is not in a diffusion-limited regime, and the electrodes are expected to show similar charge–discharge behaviour despite their significant microstrucural differences with increasing binder content (as shown in Fig. 1).[10,31] Fig. 5B shows the capacity for the same electrodes after formation at charge–discharge rates from 0.1C to 2C. At 0.5C the 4 wt% electrode showed a reduced capacity, which degraded more significantly at 1C and 2C. The 0.5 wt% PTFE electrode had 5%, 43% and 151% better capacity retention than the 4 wt% electrode at charge–discharge rates of 0.5C, 1C and 2C respectively. At 2C, the 2 wt% PTFE electrode also

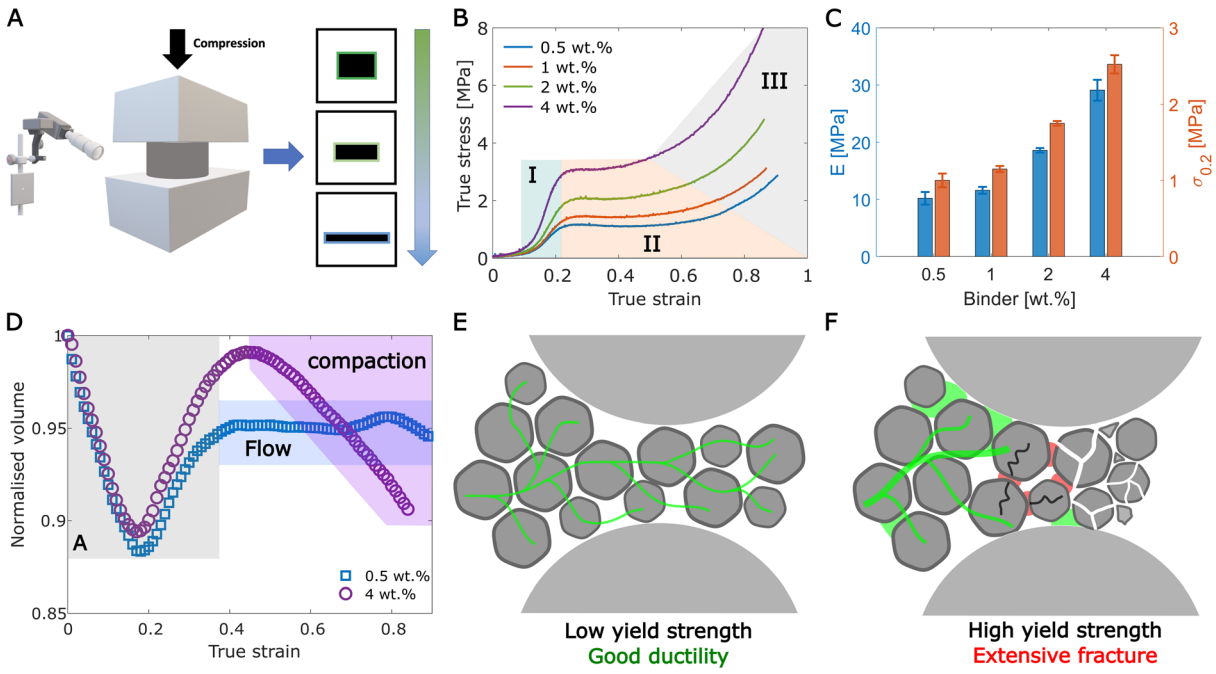

Fig. 4 (A) Schematic of the uniaxial compression and direct image correlation set up used to measure the mechanical properties of electrode disks (2 mm height × 5 mm in diameter). (B) True stress–true strain curves of 0.5, 1, 2 and 4 wt% PTFE electrode disks. (C) Young's modulus and 0.2% proof stress of these disks. (D) Normalised volume evolution with deformation during uniaxial compression of the 0.5 and 4 wt% electrode disks. (E and F) Schematics showing the deformation behaviour for low and high binder electrodes during calendering.

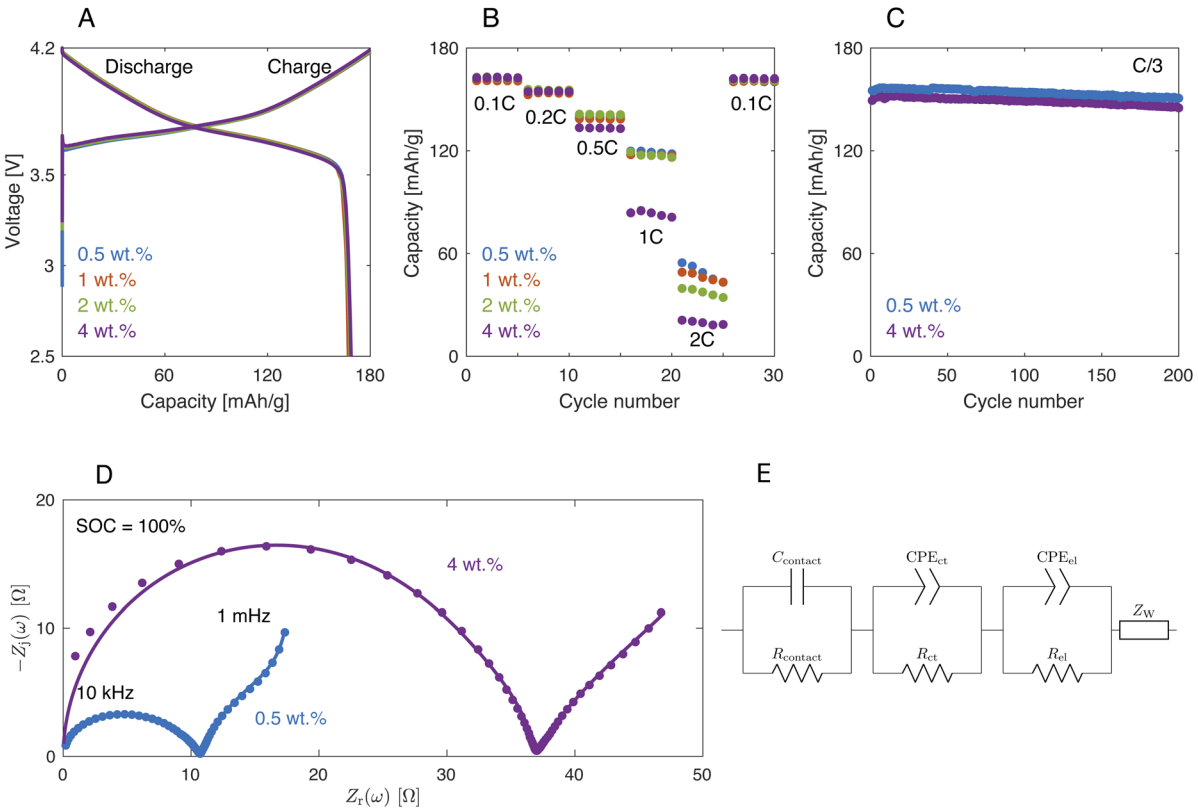

Fig. 5 (A) First charge–discharge cycle (C/20) of solvent-free NMC electrodes containing 0.5, 1, 2 and 4 wt% PTFE. (B) Capacity of solvent-free NMC electrodes containing 0.5, 1, 2 and 4 wt% PTFE at charge–discharge rates up to 2C (average of 2 electrodes). (C) Long term capacity of solvent-free NMC full cells (*vs.* LTO) containing 0.5 and 4 wt% PTFE at a charge–discharge rate of C/3 (average of 2 electrodes). (D) Nyquist plots of the impedance at 100% SOC for NMC half-cells containing 0.5 and 4 wt% PTFE. (E) Equivalent circuit used to model the electrode impedance.

showed reduced capacity compared with the 0.5 wt% and 1 wt% PTFE electrodes.

Long-term cycling stability is presented in Fig. 5C for the 0.5 wt% and 4 wt% electrodes, showing very similar capacity retention of 97% and 96.7%, respectively, after 200 cycles at C/3. This is consistent with the C rates data shown in Fig. 5B, and suggests that for relatively low C-rates (≤C/3), the long-term cycling stability remains excellent, even for binder content as low as 0.5 wt%.

Fig. 5D compares the EIS spectra of the electrodes containing 0.5 and 4 wt% PTFE. The data was fitted to the equivalent circuit shown in Fig. 5E, and the extracted best-fit parameters are summarised in Table 1. The impedance curves were composed of two overlapping semi-circles at high frequency, followed by a third semi-circle ending in an upward tail at low frequency. These features were matched to specific materials parameters by performing a system identification analysis at different state-of-charges (SOC) for a typical electrode (summarised in Fig. S.5 and Table S.2†). More information about the collected impedance data and model is available in ESI.† The first semi-circle at the highest frequency was attributed to the contact resistance ($R_{contact}$) between the electrode and current collector, which was consistent with previous reports on similar materials and supported by a near constant value at different SOC.[32] The second semi-circle at intermediate frequency increased in radius with decreasing SOC, corresponding to the charge transfer resistance (R_{ct}).[33,34] The final semi-circle at lower frequency was attributed to the ionic diffusion in the electrolyte (R_{el}), and the tail at the lowest frequency corresponded to solid-state diffusion in the active material (R_w).

Table 1 indicates that R_{el} and $R_{contact}$ were significantly higher (3× and 10× respectively) for the 4 wt% PTFE electrode. This is consistent with the SEM analysis in Fig. 1 and 2 that revealed a drastic reduction in surface porosity and the presence of large bulk PTFE regions in the 4 wt% electrode. This microstructure is likely to cause a significant reduction in ionic mobility and electronic conductivity, as confirmed by the EIS analysis. The electronic conductivity of the solvent-free electrodes was also measured with a four point probe instrument. The electronic conductivity decreased from 17.7 S m^{-1} to 10.4 S

Table 1 Resistances from equivalent circuit analysis and corresponding to the best-fit impedance curves in Fig. 5D. All parameters are listed in Table S.3

Electrode	$R_{contact}$ [Ω]	R_{ct} [Ω]	R_{el} [Ω]	R_w [Ω]
0.5 wt% PTFE	3.1	7.5	6.7	5.8
4 wt% PTFE	30	6.4	21	4.7

m^{-1} for the 0.5 wt% and 4 wt% electrodes, respectively (Fig. S.6†).

3 Conclusion

In summary, we have shown that the fraction of PTFE binder has a large impact on the inter-related aspects of processability, final microstructure and performance of solvent-free LIB electrodes. From a microstructural perspective, above 2 wt% binder, PTFE begins to block critical electrode porosity, hindering charge carrying ionic mobility through the electrode, and also lowers its electronic conductivity. Higher binder fractions lead to excessive load transferred to active material particles, causing active material fracture during calendering. In contrast, lower fractions of PTFE allow compaction at relatively low stress that avoids widespread particle fracture. Quantitatively, increasing PTFE from 0.5 wt% to 4 wt% dramatically increased the electrode stiffness from 10 MPa to 30 MPa and yield strength from 1 MPa to 2.5 MPa. Electrochemically, the 0.5 wt% PTFE electrode showed superior capacity retention at higher charge–discharge rate, with improvements of up to 150% at 2C compared with the 4 wt% PTFE electrode. The strong interplay between electrode formulation, mechanical properties and microstructure, which ultimately impacts electrochemical performance, suggests that active materials developed for slurry casting may not always be suitable for solvent-free processing. This offers an opportunity to design active material particles more resistant to fracture and overall formulations better suited to solvent-free manufacturing. The novel mechanical testing methodology developed here combined with advanced electrode characterisation techniques can be applied to other systems and guide the design of new electrode manufacturing processes for Li-ion and beyond Li-ion batteries.

4 Materials and methods

4.1 Materials

The positive electrode active material used in all electrodes was $LiNi_{0.6}Mn_{0.2}Co_{0.2}O_2$ (NMC622) powder with a median particle size of 10 μm (Targray, Canada) and a typical discharge capacity of 175 mA h g^{-1} when cycled between 2.8 and 4.25 V. The polytetrafluoroethylene (PTFE) powder had a particle size between 100 and 200 μm (3M, Germany) and the carbon nano fibres (CNF) for electrical conduction had an average diameter of 150–200 nm and a length of several tens of μm (Pyrograf, USA).

4.2 Electrode preparation

For the solvent-free manufacture of electrodes, the active material, binder and CNF were mixed together in a Thinky planetary mixer for 6 minutes from 300 up to 2000 rpm before being transferred to an agate mortar. The mortar containing the mixed powders and the pestle were subsequently heated in an oven at 80 °C for 20 min, and then mixed manually. After 5 min, a single integral flake was obtained, and further kneaded for 5 min. The flake was then calendered at a temperature of 80 °C and a line pressure from 50 up to 100 N mm^{-1} to obtain a thickness of approximatively 100 μm using a SUMET CA3 hot calendar. The $Li_4Ti_5O_{12}$ (LTO) (median particle size 5–10 μm, MSE, USA) counter anodes used in full cells were fabricated using the same solvent-free process.

4.3 Coin cell assembly

Disks of 14 mm diameter were punched out of the calendered electrodes and dried overnight in a vacuum oven (flushed with Ar) at 120 °C. All the solvent-free cathodes had a thickness in the range 100–110 μm and an areal loading of 30–33 mg cm^{-2} (see Table S.4†). CR2032 half-cells were assembled with the cathode working against a cleaned and flattened Li chip. CR2032 full-cells were made with the cathode working against the LTO anode. A glass fibres separator (Whatman, USA) was used and the electrolyte was 1 M $LiPF_6$ in ethylene carbonate and dimethyl carbonate (EC/EMC 3/7) + 2 wt% VC (Elyte, Germany). 140 and 180 μL of electrolyte was used in the half-cells and full-cells, respectively. For the full-cells, the cathodes were matched with anodes to give an areal and gravimetric capacity ratio of approximatively 1 : 1.1. The coin-cell assembly was performed in a glove box under a high purity Ar atmosphere (O_2 < 0.1 ppm) and all the components were dried overnight under vacuum in an antechamber at 80 °C. The coin cells were firmly crimped before being taken out of the glovebox for testing. Three electrodes cells were also prepared for electrochemical impedance spectroscopy (EIS) using El-cell PAT cells with a Li reference electrode and a Li chip as the counter electrode.

4.4 Electrochemical characterisation

Coin cells were tested using a battery cycler (Arbin Instruments, USA) in the potential range of 2.5–4.2 V for NMC-based half-cells at room temperature. The NMC-LTO full cells were cycled in the potential range of 1–2.8 V at room temperature and at a C-rate of C/3. The cells were formed by performing two charge–discharge cycles at C/20 followed by two further cycles at C/10. The cells were charged using a standard CC-CV protocol (the cut-off current was half the current used in the CC step) followed by a CC discharge.

Impedance measurements were taken at room temperature using a Biologic VSP potentiostat (measurement accuracy ±0.1%), over the frequency range 1 mHz–10 kHz with 10 frequencies per decade and a nominal AC voltage amplitude of 10 mV. Every EIS measurement was performed after a relaxation period of 2 h to allow the electrode to reach steady-state (additional information is available in ESI†).

The electronic conductivity of the electrodes were measured using an Ossila four probe instrument. At least six electrodes (8 mm in diameter) were measured and the average value and standard deviation were computed.

4.5 Microstructure characterisation

The scanning electron microscopy (SEM) and energy dispersive X-ray (EDX) analysis were performed with a high-resolution Merlin field emission scanning electron microscope (Zeiss, Germany) equipped with an EDX X-max detector (Oxford Instruments, UK) at an accelerating voltage of 2–3 kV.

The XRD analysis was performed using a Panalytical Empyrean X-ray diffractometer equipped with a Cu source operated at 40 kV and 40 mA. The Rietveld refinement was performed using the HighScore Plus software. Instrument broadening was corrected using a Si reference.

The transmission electron microscopy (TEM) samples were prepared using the same solvent-free process described above. NMC was replaced by NaCl which was subsequently dissolved to preserve only the PTFE fibril network. A 3 mm disk of the NaCl electrode was cut with a biopsy punch and then pressed onto a carbon coated copper TEM grid with a glass slide. The TEM sample was then immersed into water overnight to dissolve and remove NaCl from the electrode and leave only the PTFE fibril network onto the copper grid. This method enabled to obtain samples that are electron transparent and suitable for transmission electron microscopy. The TEM analysis was performed with a Jeol 2100 TEM (W source) operated at 200 kV and equipped with a Gatan Metro *In Situ* Counting Camera. Porosity was estimated from relative density measurements performed on 14 mm disks cut from calendered electrode sheets. The density was estimated by measuring the mass of the disk and its dimensions with a micrometer.

4.6 Mechanical testing

Compression tests were performed using a DEBEN universal testing machine equipped with a 1 kN load cell and stainless steel compression jaws. All compression tests were performed at 80 °C (same as the calendering temperature) on cylindrical specimens of 2 mm thickness and 5 mm diameter at a crosshead speed of 0.4 mm min^{-1}, corresponding to an engineering strain rate of 0.2 min^{-1}. The dimensions of the specimens were captured with a high resolution camera and extracted *via* an image processing algorithm developed in MATLAB and based on the code available here: **https://github.com/EdDarnbrough/DEBEN-and-ThorCam**.

Data availability

Data will be made available on request.

Author contributions

Guillaume Matthews: conceptualization, investigation, formal analysis, methodology, writing – original draft. Benjamin Meyer: investigation, writing – review and editing. Chris Doerrer: resources, writing – review and editing. Julia Ramírez-González: formal analysis, writing – review and editing Ed Darnbrough: software, writing – review and editing. Noël Hallemans: software, formal analysis, writing – review and editing. David Armstrong: resources, writing – review and editing. Patrick Grant: resources, supervision, writing – review and editing.

Conflicts of interest

There are no conflicts to declare.

Acknowledgements

The authors would like to thank the Faraday Institution for financial support through grant "Nextrode – next generation electrodes" (FIRG015 and FIRG066) and SOLBAT (FIRG026 and FIRG056). The authors acknowledge the use of characterisation facilities within the David Cockayne Centre for Electron Microscopy, Department of Materials, University of Oxford.

References

1 P. S. Grant, D. Greenwood, K. Pardikar, *et al.*, Roadmap on li-ion battery manufacturing research, *JPhys Energy*, 2022, **4**, 042006, DOI: **10.1088/2515-7655/ac8e30**.
2 W. B. Hawley, A. Parejiya, Y. Bai, H. M. Meyer, D. L. Wood and J. Li, Lithium and transition metal dissolution due to aqueous processing in lithium-ion battery cathode active materials, *J. Power Sources*, 2020, **466**, 228315, DOI: **10.1016/j.jpowsour.2020.228315**.
3 Y. Liu, R. Zhang, J. Wang and Y. Wang, Current and future lithium-ion battery manufacturing, *iScience*, 2021, **24**, 102332, DOI: **10.1016/j.isci.2021.102332**.
4 B. Ludwig, Z. Zheng, W. Shou, Y. Wang and H. Pan, Solvent-free manufacturing of electrodes for lithium-ion batteries, *Sci. Rep.*, 2016, **6**, 23150, DOI: **10.1038/srep23150**.
5 D. J. Kirsch, S. D. Lacey, Y. Kuang, *et al.*, Scalable dry processing of binder-free lithium-ion battery electrodes enabled by holey graphene, *ACS Appl. Energy Mater.*, 2019, **2**, 2990–2997, DOI: **10.1021/acsaem.9b00066**.
6 G. Schälicke, I. Landwehr, A. Dinter, K. H. Pettinger, W. Haselrieder and A. Kwade, Solvent-free manufacturing of electrodes for lithium-ion batteries *via* electrostatic coating, *Energy Technol.*, 2020, **8**, 1900309, DOI: **10.1002/ente.201900309**.
7 Y. Lu, C. Z. Zhao, H. Yuan, J. K. Hu, J. Q. Huang and Q. Zhang, Dry electrode technology, the rising star in solid-state battery industrialization, *Matter*, 2022, **5**(3), 876–898, DOI: **10.1016/j.matt.2022.01.011**.
8 Y. Zhang, S. Lu, Z. Wang, V. Volkov, F. Lou and Z. Yu, Recent technology development in solvent-free electrode fabrication for lithium-ion batteries, *Renewable Sustainable Energy Rev.*, 2023, **183**, 113515, DOI: **10.1016/j.rser.2023.113515**.
9 R. Tao, B. Steinhoff, X. G. Sun, *et al.*, High-throughput and high-performance lithium-ion batteries *via* dry processing, *Chem. Eng. J.*, 2023, **471**, 144300, DOI: **10.1016/j.cej.2023.144300**.
10 G. Matthews, S. Wheeler, J. Ramírez-González and P. S. Grant, Solvent-free nmc electrodes for li-ion batteries: Unravelling the microstructure and formation of the ptfe nano-fibril network, *Front. Energy Res.*, 2023, **11**, DOI: **10.3389/fenrg.2023.1336344**.
11 Y. Liu, X. Gong, C. Podder, *et al.*, Roll-to-roll solvent-free manufactured electrodes for fast-charging batteries, *Joule*, 2023, **7**, 952–970, DOI: **10.1016/j.joule.2023.04.006**.
12 M. Forytta, Environmentally friendly manufacture of battery electrodes sustainable battery production, Sep. 2021. [Online]. Available: **https://www.iws.fraunhofer.de**.

13 M. Forytta, Drytraec to become technology platform, May 2022. [Online]. Available: https://www.iws.fraunhofer.de.
14 M. Ank, A. Sommer, K. A. Gamra, *et al.*, Lithium-ion cells in automotive applications: Tesla 4680 cylindrical cell teardown and characterization, *J. Electrochem. Soc.*, 2023, **170**, 120536, DOI: 10.1149/1945-7111/ad14d0.
15 M. K. Sadan, G. J. Lian, R. M. Smith and D. Cumming, Co, ni-free ultrathick free-standing dry electrodes for sustainable lithium-ion batteries, *ACS Appl. Energy Mater.*, 2023, **6**, 12166–12171, DOI: 10.1021/acsaem.3c02448.
16 Y. Zhang, F. Huld, S. Lu, C. Jektvik, F. Lou and Z. Yu, Revisiting polytetrafluorethylene binder for solvent-free lithium-ion battery anode fabrication, *Batteries*, 2022, **8**, 57, DOI: 10.3390/batteries8060057.
17 V. Manev, I. Naidenov, B. Puresheva, P. Zlatilova and G. Pistoia, Electrochemical performance of natural brazilian graphite as anode material for lithium-ion rechargeable cells, *J. Power Sources*, 1995, **55**(2), 211–215.
18 H. Zhou, M. Liu, H. Gao, *et al.*, Dense integration of solvent-free electrodes for li-ion supercabattery with boosted low temperature performance, *J. Power Sources*, 2020, **473**, 228553, DOI: 10.1016/j.jpowsour.2020.228553.
19 H. Oh, G. S. Kim, B. U. Hwang, J. Bang, J. Kim and K. M. Jeong, Development of a feasible and scalable manufacturing method for ptfe-based solvent-free lithium-ion battery electrodes, *Chem. Eng. J.*, 2024, **491**, 151957, DOI: 10.1016/j.cej.2024.151957.
20 J. Kim, K. Park, M. Kim, *et al.*, 10 mah cm-2 cathode by roll-to-roll process for low cost and high energy density li-ion batteries, *Adv. Energy Mater.*, 2024, **14**, 2303455, DOI: 10.1002/aenm.202303455.
21 G. Park, H. S. Kim and K. J. Lee, Solvent-free processed cathode slurry with carbon nanotube conductors for li-ion batteries, *Nanomaterials*, 2023, **13**, 324, DOI: 10.3390/nano13020324.
22 W. Yao, M. Chouchane, W. Li, *et al.*, A 5 v-class cobalt-free battery cathode with high loading enabled by dry coating, *Energy Environ. Sci.*, 2023, **16**, 1620–1630, DOI: 10.1039/d2ee03840d.
23 F. Hippauf, B. Schumm, S. Doerfler, *et al.*, Overcoming binder limitations of sheet-type solid-state cathodes using a solvent-free dry-film approach, *Energy Storage Mater.*, 2019, **21**, 390–398, DOI: 10.1016/j.ensm.2019.05.033.
24 C. Doerrer, M. Metzler, G. Matthews, *et al.*, Spraying li6ps5cl and silver-carbon multilayers to facilitate large-scale fabrication of all-solid-state batteries, *Device*, 2024, 100468, DOI: 10.1016/j.device.2024.100468. [Online]. Available: https://linkinghub.elsevier.com/retrieve/pii/S2666998624003430.
25 M. Singh, J. Kaiser and H. Hahn, Thick electrodes for high energy lithium ion batteries, *J. Electrochem. Soc.*, 2015, **162**, A1196–A1201, DOI: 10.1149/2.0401507jes.
26 K. Sato, Y. Tominaga, Y. Imai, T. Yoshiyama and Y. Aburatani, Deformation capability of poly(tetrafluoroethylene) materials: Estimation with x-ray diffraction measurements, *Polym. Test.*, 2022, **113**, 107690, DOI: 10.1016/j.polymertesting.2022.107690.
27 D. Dang, Y. Wang and Y.-T. Cheng, Communication—fracture behavior of single lini 0.33 mn 0.33 co 0.33 o 2 particles studied by flat punch indentation, *J. Electrochem. Soc.*, 2019, **166**, A2749–A2751, DOI: 10.1149/2.0331913jes.
28 A. Wade, A. V. Llewellyn, T. M. M. Heenan, *et al.*, First cycle cracking behaviour within ni-rich cathodes during high-voltage charging, *J. Electrochem. Soc.*, 2023, **170**, 070513, DOI: 10.1149/1945-7111/ace130.
29 I. Duarte, M. Vesenjak and L. Krstulović-Opara, Compressive behaviour of unconstrained and constrained integral-skin closed-cell aluminium foam, *Compos. Struct.*, 2016, **154**, 231–238, DOI: 10.1016/j.compstruct.2016.07.038.
30 R. J. Arsenault, *Treatise on Materials Science and Technology: Plastic Deformation of Materials*, Elsevier, 1st edn, 1975, vol. 6.
31 M. J. Lain and E. Kendrick, Understanding the limitations of lithium ion batteries at high rates, *J. Power Sources*, 2021, **493**, 229690, DOI: 10.1016/j.jpowsour.2021.229690.
32 J.-M. Atebamba, J. Moskon, S. Pejovnik and M. Gaberscek, On the interpretation of measured impedance spectra of insertion cathodes for lithium-ion batteries, *J. Electrochem. Soc.*, 2010, **157**, A1218, DOI: 10.1149/1.3489353.
33 R. Scipioni, P. S. Jørgensen, C. Graves, J. Hjelm and S. H. Jensen, A physically-based equivalent circuit model for the impedance of a lifepo 4/graphite 26650 cylindrical cell, *J. Electrochem. Soc.*, 2017, **164**, A2017–A2030, DOI: 10.1149/2.1071709jes.
34 B. Csomós and D. Fodor, Identification of the material properties of an 18650 li-ion battery for improving the electrochemical model used in cell testing, *Hung. J. Ind. Chem.*, 2020, **48**, 33–41, DOI: 10.33927/hjic-2020-06.